catalysts

MDPI

Article

Design and Preparation of $ZnIn_2S_4$/g-C_3N_4 Z-Scheme Heterojunction for Enhanced Photocatalytic CO_2 Reduction

Jinghong Fang, Min Wang, Xiaotong Yang, Qiong Sun * and Liyan Yu *

College of Materials Science and Engineering, Qingdao University of Science and Technology, Qingdao 266042, China

* Correspondence: sunqiong@qust.edu.cn (Q.S.); liyanyu@qust.edu.cn (L.Y.)

Abstract: In this study, a novel Z-scheme heterojunction photocatalyst was developed by integrating g-C_3N_4 nanoplates into $ZnIn_2S_4$ microspheres. X-ray photoelectron spectroscopy analysis revealed a directional electron transfer from g-C_3N_4 to $ZnIn_2S_4$ upon heterojunction formation. Under irradiation, electrochemical tests and electron paramagnetic resonance spectroscopy demonstrated significantly enhanced charge generation and separation efficiencies in the $ZnIn_2S_4$/g-C_3N_4 composite, accompanied by reduced charge transfer resistance. In photocatalytic CO_2 reduction, the $ZnIn_2S_4$/g-C_3N_4 composite achieved the highest CO yield, 1.92 and 5.83 times higher than those of pristine g-C_3N_4 and $ZnIn_2S_4$, respectively, with a notable CO selectivity of 91.3% compared to H_2 (8.7%). The Z-scheme heterojunction mechanism, confirmed in this work, effectively preserved the strong redox capabilities of the photoinduced charge carriers, leading to superior photocatalytic performance and excellent long-term stability. This study offers valuable insights into the design and development of g-C_3N_4-based heterojunctions for efficient solar-driven CO_2 reduction.

Keywords: $ZnIn_2S_4$/g-C_3N_4; photocatalytic CO_2 reduction; z-type heterojunction

check for updates

Academic Editor: Narendra Kumar

Received: 4 December 2024
Revised: 30 December 2024
Accepted: 16 January 2025
Published: 20 January 2025

Citation: Fang, J.; Wang, M.; Yang, X.; Sun, Q.; Yu, L. Design and Preparation of $ZnIn_2S_4$/g-C_3N_4 Z-Scheme Heterojunction for Enhanced Photocatalytic CO_2 Reduction. *Catalysts* **2025**, *15*, 95. https://doi.org/10.3390/catal15010095

1. Introduction

With the rapid development of modern industry, the emission of CO_2 and other greenhouse gasses has increased significantly, contributing to global warming and posing a severe threat to the survival of humans and other organisms [1,2]. Compared to conventional carbon dioxide capture strategies, such as physical adsorption and geological storage, which are often associated with high energy consumption, the conversion or reuse of CO_2 offers a more sustainable and promising approach. This strategy not only addresses energy and environmental challenges, but also holds significant potential for practical and feasible applications [3–5].

Various technologies have been developed to convert CO_2 into hydrocarbons or high-value-added chemicals, including thermal catalysis, biocatalysis, photoelectrocatalysis, electrocatalysis, and photocatalytic reduction [6,7]. Converting CO_2 into CO and other useful low-carbon fuels in a renewable and environmentally friendly manner not only helps reduce atmospheric CO_2 concentrations but also facilitates "closed-loop" carbon fixation. Among these methods, the photocatalytic reduction of CO_2, which mimics the natural photosynthesis process, uses solar energy and photocatalysts (artificial photosynthesis) to catalytically convert CO_2 and H_2O into solar fuels and high-value chemicals, such as C1 products (CO, CH_4, CH_3OH, HCOOH) and C2 products (C_2H_4, C_2H_6, C_3H_6, C_2H_5OH) [8,9].

However, despite the demonstrated activity of various semiconductor photocatalysts for CO_2 reduction, their practical applications are hindered by the slow separation and transport kinetics of photogenerated carriers and poor product selectivity. These limitations necessitate further advancements [10,11]. Among photocatalysts, graphite-phase carbon nitride (g-C_3N_4) has gained attention due to its visible light response (bandgap of about 2.7 eV), non-toxicity, good biocompatibility, excellent chemical and thermal stability, and ease of synthesis. These properties make g-C_3N_4 suitable for applications such as water splitting for hydrogen production, artificial photosynthesis, the degradation of organic pollutants, and CO_2 reduction [12–14]. Like most photocatalysts, pure g-C_3N_4 synthesized via conventional calcination suffers from rapid electron–hole recombination and limited exposed active sites. These shortcomings can be addressed through nanostructure modification, heterojunction construction, or combination with cocatalysts. Among these strategies, constructing heterojunction structures has proven to be one of the most effective methods for enhancing photocatalytic performance due to its ability to facilitate efficient electron–hole pair separation and transfer [15,16]. For example, Luo et al. [17] prepared ultrathin $CsPbBr_3$/g-C_3N_4 nanosheets using a simple electrostatic self-assembly process. Under AM 1.5 G light source irradiation, these nanosheets effectively reduced CO_2 to CH_4 and CO. In situ X-ray photoelectron spectroscopy (XPS) revealed a direct Z-scheme charge transfer mechanism at the $CsPbBr_3$ and g-C_3N_4 interface, achieving efficient charge separation and high redox potential.

Zinc indium sulfide ($ZnIn_2S_4$, ZIS), a chemically stable and non-toxic material, possesses suitable energy band positions (2.06–2.85 eV) for the reduction of CO_2 into hydrocarbon fuels. However, a high charge recombination rate and a short lifetime of photogenerated electrons caused by the bandgap limit its photocatalytic efficiency [18,19]. The formation of heterojunctions by combining $ZnIn_2S_4$ with other wide bandgap semiconductors has been widely recognized as an effective strategy to enhance photocatalytic performance [20–22].

Shao et al. [23] constructed a 3D/2D g-C_3N_4/$ZnIn_2S_4$ hollow spherical heterostructure by growing modified $ZnIn_2S_4$ nanosheets on the surface of g-C_3N_4 microspheres. This composite material combines the advantages of a hollow structure, including enhanced light absorption and increased active sites, with the heterostructure's ability to improve photogenerated electron migration and separation. These features effectively address the significant issue of photogenerated electron recombination observed in the individual components. Similarly, Chen et al. [24] fabricated a spatial distribution heterojunction via the in situ growth of $ZnIn_2S_4$ nanosheets (ZIS) on g-C_3N_4 microtubes (T-CN), which demonstrated excellent performance in photocatalytic CO_2 reduction. Their experimental findings revealed that the spatial distribution of ZIS nanosheets on T-CN enhances light absorption, accelerates interfacial charge transfer, and increases CO_2 adsorption capacity, collectively contributing to the superior catalytic activity of the composite.

In this study, two-dimensional g-C_3N_4 nanoplates were integrated with $ZnIn_2S_4$ featuring a distinctive nanoflower structure using a simple mechanical stirring method. The photocatalytic activity and stability of the resulting $ZnIn_2S_4$/g-C_3N_4 composite were systematically evaluated in CO_2 reduction reactions. The findings revealed that the $ZnIn_2S_4$/g-C_3N_4 heterojunction significantly outperformed pure g-C_3N_4 nanoplates and $ZnIn_2S_4$ nanoflowers in photocatalytic CO_2 reduction, achieving an enhanced yield. Moreover, the composite exhibited high selectivity for CO over H_2, underscoring its potential for efficient and targeted photocatalytic applications.

2. Results and Discussion

2.1. Characterization of the Samples

The crystal structures of the samples were analyzed using XRD patterns, as shown in Figure 1. Bare g-C_3N_4 exhibits two characteristic diffraction peaks at approximately 13.1° and 27.4°, corresponding to the (100) and (002) planes, respectively (JCPDS No.87-1526). These peaks represent the in-plane tri-s-triazine unit repetition and the interlayer stacking of aromatic ring structures. For $ZnIn_2S_4$ and the $ZnIn_2S_4$/g-C_3N_4 composite, five prominent diffraction peaks at 21.29°, 27.66°, 47.35°, 52.19°, and 55.57° are assigned to the (006), (102), (110), (116), and (202) planes of $ZnIn_2S_4$, respectively (JCPDS No.72-0305) [25]. In the composite, a weak diffraction peak corresponding to the g-C_3N_4 (100) plane is observed, while the (002) plane of g-C_3N_4 partially overlaps with the (102) plane of $ZnIn_2S_4$.

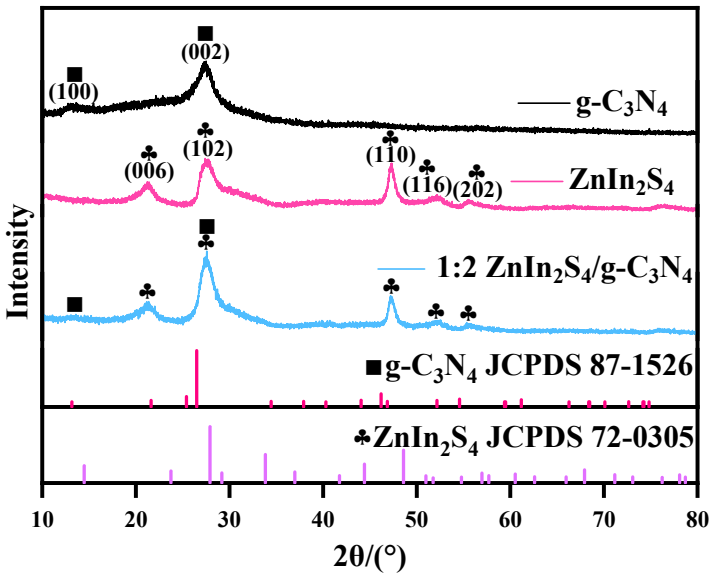

Figure 1. XRD patterns of g-C_3N_4, $ZnIn_2S_4$ and 1:2 $ZnIn_2S_4$/g-C_3N_4.

The microstructures of $ZnIn_2S_4$ and $ZnIn_2S_4$/g-C_3N_4 were examined through FESEM images. As shown in Figure 2a, $ZnIn_2S_4$ exhibits a distinct three-dimensional layered spherical nanoflower structure. In Figure 2b, the integration of $ZnIn_2S_4$ with g-C_3N_4 results in g-C_3N_4 nanosheets being inserted into the folds of the $ZnIn_2S_4$ structure, leading to a significantly rougher surface. The energy-dispersive spectroscopy (EDS) analysis (Figure 2c–h) confirms the presence of C, N, Zn, In, and S elements in the composite material. Moreover, the distribution maps reveal that the C and N elements from g-C_3N_4 are uniformly dispersed and surround the Zn, In, and S elements originating from $ZnIn_2S_4$.

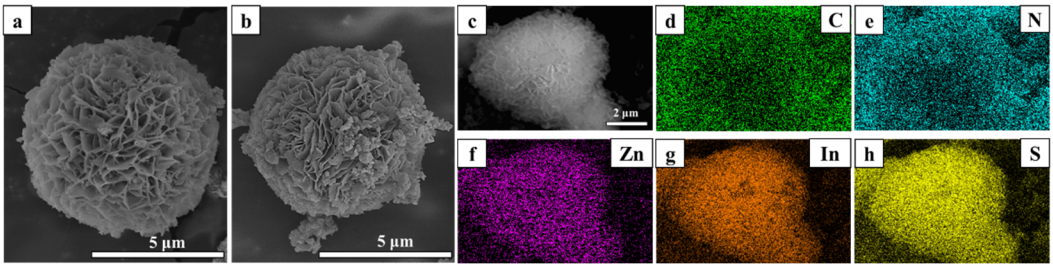

Figure 2. FESEM images of (**a**) $ZnIn_2S_4$ and (**b**) 1:2 $ZnIn_2S_4$/g-C_3N_4, along with (**c**–**h**) the corresponding elemental mappings of Zn, In, S, C, and N in 1:2 $ZnIn_2S_4$/g-C_3N_4.

XPS spectra were employed to investigate the structure and surface elemental composition of the different samples. In the full survey spectrum (Figure 3a), the elements

C, N, Zn, In, and S are detected in the $ZnIn_2S_4/g\text{-}C_3N_4$ composites, which is consistent with the EDS results. In Figure 3b, the C1s peaks in both $g\text{-}C_3N_4$ and $ZnIn_2S_4/g\text{-}C_3N_4$ can be deconvoluted into two components: one at approximately 284.8 eV corresponding to graphite carbon (C-C), and another at 288.0 eV attributed to sp^2-bonded carbon (N-C=N). Compared to pristine $g\text{-}C_3N_4$, the intensity of the N-C=N peak in $ZnIn_2S_4/g\text{-}C_3N_4$ is weaker, likely due to the shielding effect of $ZnIn_2S_4$ [24]. In Figure 3c, the N 1s spectra of $g\text{-}C_3N_4$ and $ZnIn_2S_4/g\text{-}C_3N_4$ exhibit three peaks at 398.4 eV, 399.9 eV, and 401.0 eV, which correspond to C-N=C, three-coordinate $C\text{-}(N)_3$, and surface amino groups, respectively. A small peak at 404.1 eV is attributed to the π-excitation of the C-N heterocyclic ring. Figure 3d–f show the XPS spectra of the constituent elements in $ZnIn_2S_4$. Specifically, the Zn 2p peaks are observed at 1044.9 eV (Zn $2p_{1/2}$) and 1021.8 eV (Zn $2p_{3/2}$), the In 3d peaks appear at 451.9 eV (In $3d_{3/2}$) and 444.3 eV (In $3d_{5/2}$), and the S 2p peaks are located at 161.6 eV (S $2p_{1/2}$) and 160.5 eV (S $2p_{3/2}$) [26]. Furthermore, by comparing the binding energy shifts in key elements before and after the combination of $ZnIn_2S_4$ and $g\text{-}C_3N_4$, electron transfer can be inferred. The binding energies of C 1s and N 1s in $ZnIn_2S_4/g\text{-}C_3N_4$ both increase by approximately 0.1 eV compared to bare $g\text{-}C_3N_4$, suggesting a decrease in electron cloud density around the $g\text{-}C_3N_4$ in the composite. In the contrast, the binding energies of Zn 2p, In 3d, and S 2p decrease by 0.2–0.7 eV, indicating an increase in electron cloud density around the $ZnIn_2S_4$ component. These XPS results provide evidence for directional electron transfer from $g\text{-}C_3N_4$ to $ZnIn_2S_4$ upon excitation by external energy. A more detailed understanding of the electron transfer pathway will be further explored using in situ XPS, ultraviolet photoelectron spectroscopy (UPS), and density functional theory (DFT) calculations in future studies [27,28].

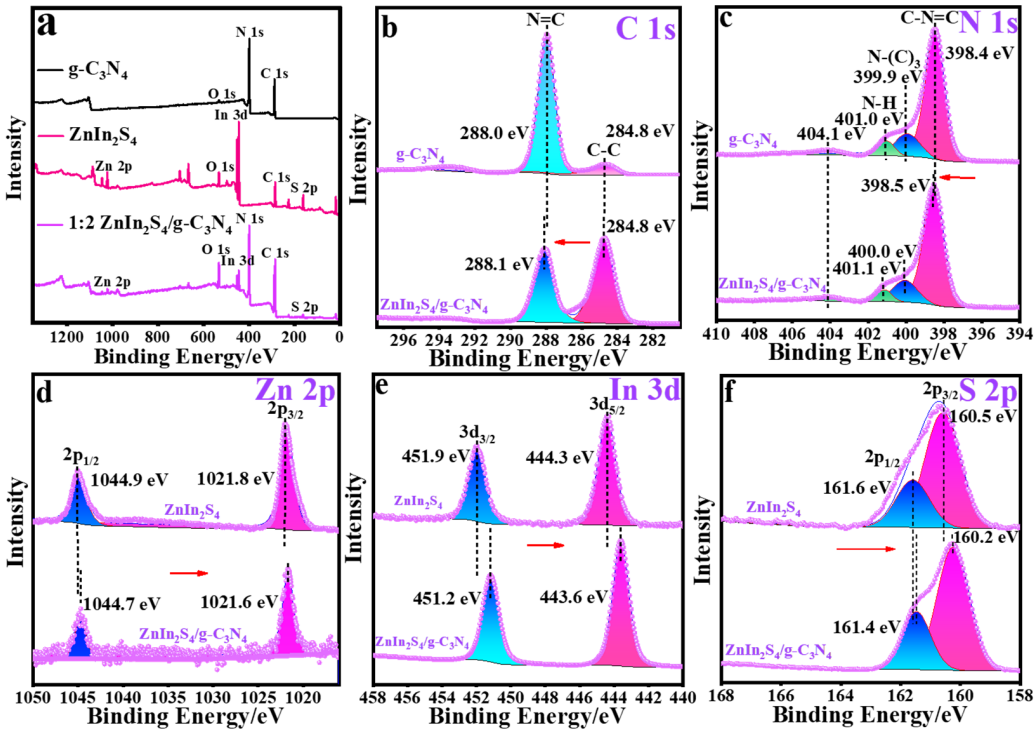

Figure 3. XPS spectra of $g\text{-}C_3N_4$, $ZnIn_2S_4$, and 1:2 $ZnIn_2S_4/g\text{-}C_3N_4$: (**a**) survey spectra, (**b**) C 1s, (**c**) N 1s, (**d**) Zn 2p, (**e**) In 3d, and (**f**) S 2p spectra.

The response ranges of different materials to incident irradiation were evaluated using UV-Vis absorption spectra. As shown in Figure 4a, the light absorption edges of pristine $g\text{-}C_3N_4$, $ZnIn_2S_4$, and the $ZnIn_2S_4/g\text{-}C_3N_4$ composite extend to approximately 430 nm, 530 nm, and 450 nm, respectively. The bandgap energy (Eg) was determined by plotting

the relationship between $(\alpha h\nu)^2$ and photon energy ($h\nu$). Based on the absorption spectra shown in Figure 4b, the calculated bandgap energies of g-C_3N_4, $ZnIn_2S_4$, and $ZnIn_2S_4$/g-C_3N_4 are 2.86 eV, 2.34 eV, and 2.74 eV, respectively. These results demonstrate that the composite material can be excited by visible light. Photoluminescence (PL) emission, which is typically attributed to the recombination of free carriers, provides insight into the degree of electron–hole recombination. Figure 4c shows the PL spectra of the materials under 320 nm excitation. The primary emission peak of pristine g-C_3N_4 is observed at 453 nm, resulting from bandgap luminescence. $ZnIn_2S_4$ exhibited the weakest PL intensity among them, reflecting its inherently poor photoluminescence properties compared to g-C_3N_4. This can be attributed to the lower total amount of photogenerated carriers produced under identical irradiation conditions. These observations are consistent with findings reported in previous studies on $ZnIn_2S_4$, g-C_3N_4, and $ZnIn_2S_4$/g-C_3N_4 composites [24,29,30]. After forming the $ZnIn_2S_4$/g-C_3N_4 composite, the significant reduction in emission peak intensity indicates that the recombination of photogenerated carriers is effectively suppressed.

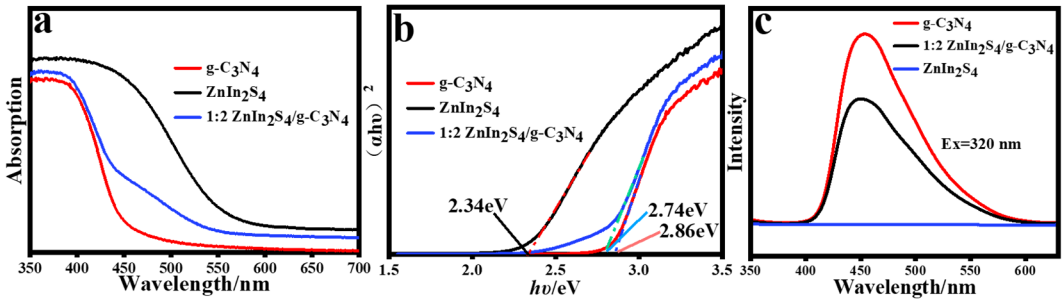

Figure 4. (**a**) UV-vis absorption spectra, (**b**) Tauc plots, and (**c**) PL spectra of g-C_3N_4, $ZnIn_2S_4$, and 1:2 $ZnIn_2S_4$/g-C_3N_4.

Electrochemical tests provide further insight into the energy band positions of the samples. Mott–Schottky (M-S) curves were employed to determine the semiconductor type and the conduction band (CB) potential. As shown in Figure 5, the positive slopes of the tangent lines drawn from the M-S curves of g-C_3N_4, $ZnIn_2S_4$, and $ZnIn_2S_4$/g-C_3N_4 confirm their n-type semiconductor characteristics. Moreover, for all three samples, the tangent lines at different test frequencies consistently intersect at the same point on the x-axis. This horizontal intercept corresponds to the flat band position (E_{fb}) of the semiconductor, which is typically approximately equal to the CB position for n-type semiconductors. After correction for the reference electrode (Ag/AgCl, +0.199 eV), the CB positions of g-C_3N_4, $ZnIn_2S_4$, and $ZnIn_2S_4$/g-C_3N_4 were determined to be −0.52 eV, −0.69 eV, and −0.63 eV, respectively.

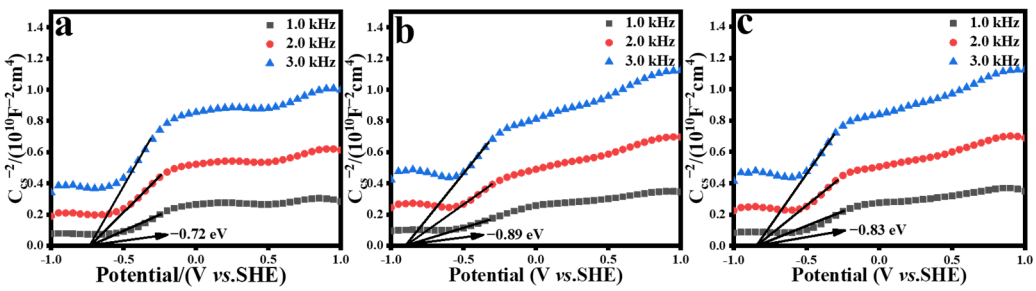

Figure 5. Mott–Schottky plots of (**a**) g-C_3N_4, (**b**) $ZnIn_2S_4$, and (**c**) 1:2 $ZnIn_2S_4$/g-C_3N_4 measured at different frequencies.

The transient photocurrent response under alternating light and dark conditions, as well as the impedance characteristics of the samples, were evaluated. As shown in Figure 6a, the $ZnIn_2S_4/g\text{-}C_3N_4$ composite exhibits the highest transient photocurrent response compared to the pristine samples, indicating improved charge separation efficiency under illumination. Additionally, EIS was used to compare the electron transfer resistance of the samples. Figure 6b shows that the Nyquist plot of $ZnIn_2S_4/g\text{-}C_3N_4$ has a significantly smaller semicircular arc diameter than those of the other two samples, indicating the lowest charge transfer resistance. This result highlights the superior photogenerated carrier transfer capability of the composite material.

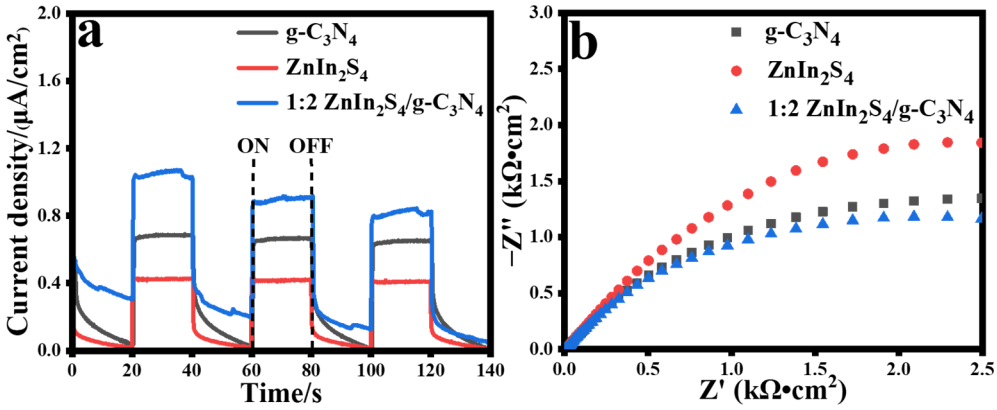

Figure 6. (**a**) Transient photocurrent response curves of $g\text{-}C_3N_4$, $ZnIn_2S_4$, and 1:2 $ZnIn_2S_4/g\text{-}C_3N_4$ under light on/off cycles. (**b**) Nyquist plots of $g\text{-}C_3N_4$, $ZnIn_2S_4$, and 1:2 $ZnIn_2S_4/g\text{-}C_3N_4$.

2.2. Photocatalytic Reduction Activity of CO_2

To validate the CO_2 reduction process, several essential blank tests were conducted. As Shown in Figure 7, a comparison between Group 1 and the control groups (Groups 2 to 4) revealed no significant production of CO or H_2 in the latter three groups. This indicates that no observable CO_2 transformation occurred under those conditions. These results confirm that the production of CO and H_2 in Group 1 is solely attributed to the photocatalytic reduction of CO_2 facilitated by the 1:2 $ZnIn_2S_4/g\text{-}C_3N_4$ composite.

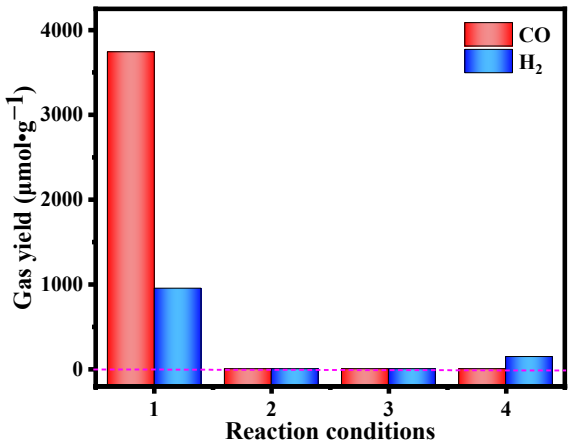

Figure 7. CO_2 reduction performance under various conditions: (1) photocatalytic CO_2 reduction using a 1:2 $ZnIn_2S_4/g\text{-}C_3N_4$ composite under light irradiation; (2) reaction with light and CO_2 but without the catalyst; (3) reaction without light, but with the catalyst and CO_2; (4) reaction with light and the catalyst, where CO_2 is replaced by Ar.

The photocatalytic properties of the g-C_3N_4, $ZnIn_2S_4$, and $ZnIn_2S_4$/g-C_3N_4 heterojunction were evaluated through the photocatalytic reduction of CO_2, with the primary gas products (CO and H_2) monitored over an eight-hour irradiation period. Figure 8a compares the photocatalytic performance of pristine g-C_3N_4, $ZnIn_2S_4$, and $ZnIn_2S_4$/g-C_3N_4 composites with various mass ratios. After 8 h of irradiation, all composite samples displayed significantly higher CO_2 reduction product yields than pure g-C_3N_4 or $ZnIn_2S_4$, demonstrating the superior catalytic efficiency of the heterostructure. Compared to similar systems listed in Table 1, the $ZnIn_2S_4$/g-C_3N_4 heterojunction demonstrates exceptional high photocatalytic performance, further highlighting its superiority and effectiveness [24,31–34]. With increasing mass ratios of $ZnIn_2S_4$ to g-C_3N_4, the product yields initially increased, reaching a maximum at a 1:2 ratio, and then decreased. The best-performing composite achieved a high selectivity for CO (91.3%) over H_2 (8.7%) and a maximum CO yield of 3743.14 μmol·g^{-1}, which is 1.92 and 5.83 times higher than those of pristine g-C_3N_4 (1941.49 μmol·g^{-1}) and $ZnIn_2S_4$ (641.68 μmol·g^{-1}), respectively. The reduced efficiency at higher loading is likely due to material agglomeration and light shielding, which hinder photogenerated carrier separation and reaction progress.

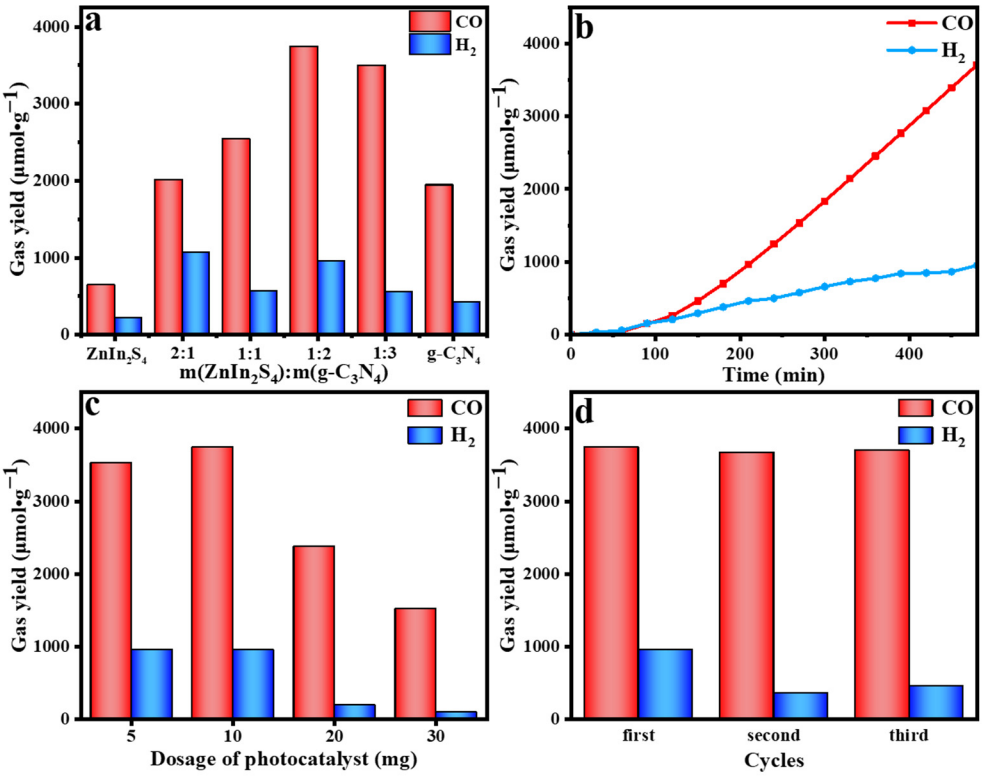

Figure 8. (**a**) Photocatalytic performance of the catalyst with varying mass ratios of $ZnIn_2S_4$ to g-C_3N_4; (**b**) time-dependent gas yield for the 1:2 $ZnIn_2S_4$/g-C_3N_4; (**c**) photocatalytic performance of the composite materials at different dosages; (**d**) results of the cyclic stability experiments.

As shown in Figure 8b, CO and H_2 were continuously produced during the CO_2 reduction process. Figure 8c explores the effect of photocatalyst loading on CO_2 reduction. The yields of CO and H_2 exhibit a volcano-shaped trend with increasing amounts of $ZnIn_2S_4$/g-C_3N_4 coated on the glass plate, reaching the maximum at a photocatalyst dosage of 10 mg.

For practical applications, the long-term photocatalytic stability of $ZnIn_2S_4$/g-C_3N_4 was assessed in cyclic experiments (Figure 8d). Over three cycles, the CO yield remained stable after each 8 h reaction period, demonstrating excellent durability of the $ZnIn_2S_4$/g-C_3N_4

composite. These results further confirm the stability and potential of the heterojunction for long-term photocatalytic CO_2 reduction applications.

Table 1. Comparison of photocatalytic performance with other Z-scheme systems.

Catalyst	Reactant Solution	Light Source	Product	Activity	Ref.
g-C_3N_4/Au/$ZnIn_2S_4$	bpy+$CoCl_2$+TEOA+solvent (CH_3CN:H_2O=3:2)	300 W Xe lamp	CO	242.3	[31]
bulk g-C_3N_4/$ZnIn_2S_4$	CH_3CN+H_2O+TEOA	300 W Xe lamp	CO	1453	[24]
nanosheet g-C_3N_4/$ZnIn_2S_4$	CH_3CN+H_2O+TEOA	300 W Xe lamp	CO	970	[24]
microtubes g-C_3N_4/$ZnIn_2S_4$	CH_3CN+H_2O+TEOA	300 W Xe lamp	CO	342	[24]
Nb doped TiO_2/g-C_3N_4	H_2O	30 W white bulbs	CO	420	[32]
g-C_3N_4/$ZnIn_2S_4$	H_2O	300 W Xe lamp	CO	467.8	
$Cu_2V_2O_7$/g-C_3N_4	H_2O	20 W white bulbs	CO	166	[33]
SnS_2/S-CTFs	TEOA	300 W Xe lamp (Visible)	CO	123.6	[34]

2.3. Photocatalytic Mechanism of $ZnIn_2S_4$/g-C_3N_4 Heterojunction

Electron paramagnetic resonance (EPR) spectroscopy was employed to identify the active radicals generated during the reaction. TEMPO, a spin-labeling agent for photoinduced electrons and holes, is reduced by electrons to form hydroxylamine (TEMPOH), resulting in a suppression of TEMPO's EPR signals [35]. As shown in Figure 9, under dark conditions, the sample dispersed in water with soluble TEMPO exhibits a characteristic triple-splitting peak with an intensity ratio of 1:1:1. Upon 30 s of xenon light irradiation, the peak intensities in both the g-C_3N_4 and $ZnIn_2S_4$/g-C_3N_4 samples significantly decrease, indicating the generation of photoinduced electrons. Notably, the reduction in peak intensity is much greater for $ZnIn_2S_4$/g-C_3N_4 than for bare g-C_3N_4. This result provides compelling evidence of the enhanced production of photoinduced electrons in $ZnIn_2S_4$/g-C_3N_4, correlating with its improved photocatalytic performance in CO_2 reduction.

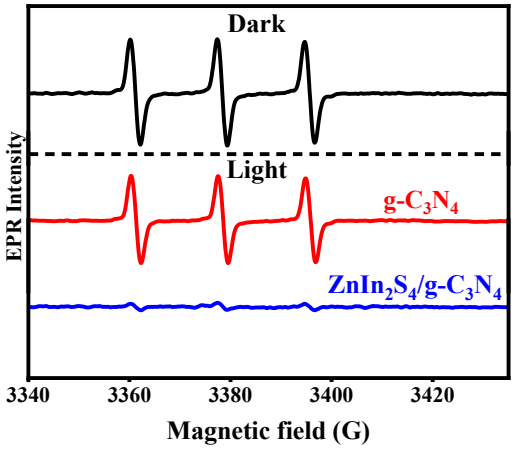

Figure 9. TEMPO spin-trapping EPR spectra of g-C_3N_4 and 1:2 $ZnIn_2S_4$/g-C_3N_4, showing photoinduced electron signals recorded in water.

Based on the experimental results, a possible mechanism for the photocatalytic reduction of CO_2 by $ZnIn_2S_4$/g-C_3N_4 is proposed and illustrated in Figure 10. Under xenon

light irradiation, electrons (e^-) in the valence band (VB) of both $ZnIn_2S_4$ and g-C_3N_4 are excited to their respective conduction band (CB), leaving behind positive holes (h^+) in the VB. Considering the CB and VB energy levels of these two semiconductors, two potential electron transfer pathways can occur between $ZnIn_2S_4$ and g-C_3N_4: the traditional Type-II heterojunction or the direct Z-scheme heterojunction. In the Type-II mechanism, excited electrons tend to transfer to the CB with the more negative potential, while holes move to the VB with the more positive potential. Although this pathway enhances the separation of charge carriers, it reduces the oxidation and reduction capabilities of the photocatalyst. Conversely, in the direct Z-scheme mechanism, electrons in the CB of one semiconductor recombine directly with holes in the VB of the other, preserving the strong reduction and oxidation abilities of the remaining charge carriers [36].

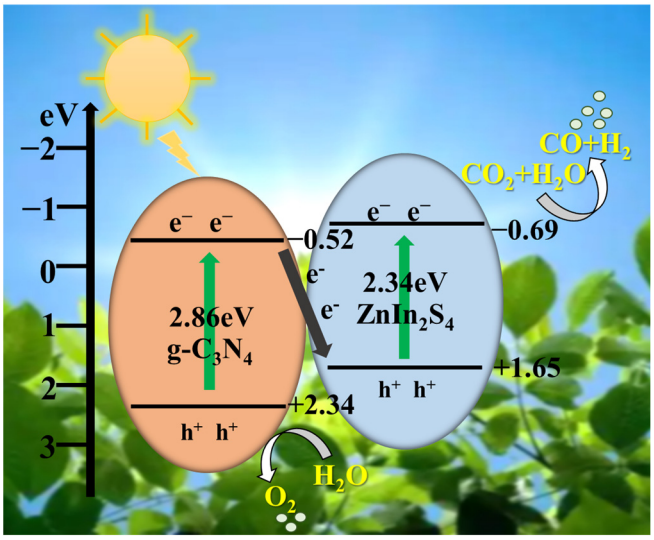

Figure 10. Proposed charge transfer mechanism for the efficient photocatalytic CO_2 reduction process facilitated by the $ZnIn_2S_4$/g-C_3N_4 heterojunction.

Evidence from XPS spectra (Figure 3) confirms electron transfer from g-C_3N_4 to $ZnIn_2S_4$, indicating the formation of a Z-scheme heterojunction in the $ZnIn_2S_4$/g-C_3N_4. Many studies [37–40] have shown that the Z-scheme configuration improves photoinduced charge generation and reduces charge transfer resistance, as corroborated by the electrochemical and EPR results in this work. Additionally, the composite exhibits a significantly suppressed recombination of photogenerated electron–hole pairs compared to its single components. In summary, the effective separation and transfer of electron–hole pairs in the Z-scheme heterojunction significantly enhance the photocatalytic CO_2 reduction performance of $ZnIn_2S_4$/g-C_3N_4.

3. Experimental

3.1. Materials

All reagents were used as received without further purification. Urea (CH_4N_2O, 99%), zinc sulfate heptahydrate ($ZnSO_4 \cdot 7H_2O$, 99.5%), ethanol (C_2H_5OH, 99.7%), and thioacetamide (C_2H_5NS, TAA, 99%) were purchased from Sinopharm Chemical Reagents Co., Ltd. (Shanghai, China). Indium chloride ($InCl_3$, 99.99%) was obtained from Shanghai Aladdin Co., Ltd. (Shanghai, China). Carbon dioxide (CO_2, 99.999%) was supplied by Qingdao Deyi Gas Co., Ltd. (Qingdao, China). 2,2,6,6-tetramethylpiperidine nitrogen oxide ($C_9H_{18}NO$, TEMPO) was purchased from Sigma Aldrich (Shanghai) Trading Co., Ltd. (Shanghai, China). Double-distilled deionized water was used throughout this study.

3.2. Preparation of g-C_3N_4

g-C_3N_4 was synthesized via a conventional calcination method [41]. Specifically, 10.0 g of urea was placed in a crucible and calcined at 550 °C for 2 h in an air atmosphere at a heating rate of 5 °C/min. After cooling to room temperature, a light-yellow powder (g-C_3N_4) was collected.

3.3. Preparation of Flower-like $ZnIn_2S_4$

$ZnIn_2S_4$ was prepared using an improved hydrothermal method based on previous reports [42]. Briefly, 1 mmol of $ZnSO_4 \cdot 7H_2O$, 2 mmol of $InCl_3$ and 2 mmol of TAA were dissolved sequentially in 60 mL of deionized water and stirred magnetically for 4.5 h. The solution was then transferred to a 100 mL Teflon-lined stainless-steel autoclave and heated at 120 °C for 2 h. After cooling to room temperature, the precipitate was washed with deionized water, centrifuged several times, and dried under vacuum at 60 °C for 12 h, yielding a yellow powder ($ZnIn_2S_4$).

3.4. Preparation of $ZnIn_2S_4$/g-C_3N_4 Composite

Firstly, y mg of g-C_3N_4 was dispersed in 300 mL of deionized water and sonicated for 30 min. Then, x mg of $ZnIn_2S_4$ was added, and the mixture was magnetically stirred at 80 °C for 2 h. The resulting yellow powder was washed with deionized water, centrifuged several times, and dried in an oven at 60 °C for 12 h. The final product was labeled as x: y $ZnIn_2S_4$/g-C_3N_4 and stored for subsequent use. The overall preparation process is illustrated in Scheme 1.

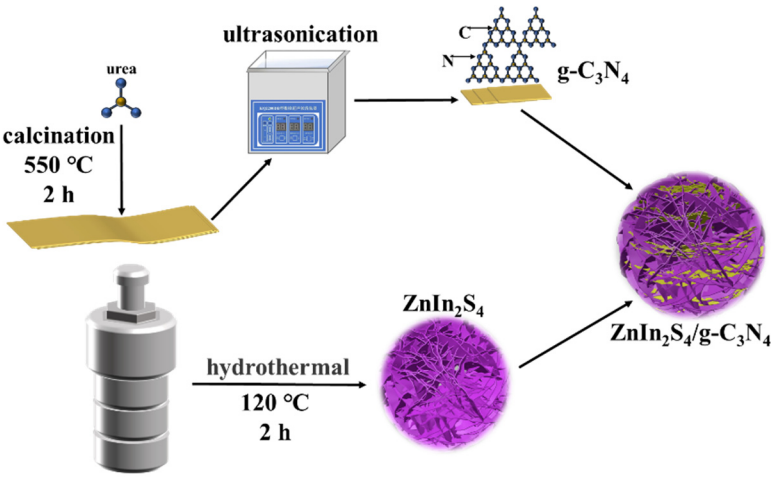

Scheme 1. The preparation process of $ZnIn_2S_4$/g-C_3N_4.

3.5. Characterizations

The crystal structure and phase composition of the samples were analyzed using an X-ray diffractometer (XRD, D/MAX-2500V, Rigaku, Tokyo, Japan) with Cu Kα radiation, scanning from 10° to 80° at a rate of 5 °min^{-1}. The morphologies of $ZnIn_2S_4$ and $ZnIn_2S_4$/g-C_3N_4 were examined using a field emission scanning electron microscope (FE-SEM, Regulus8100, Rigaku). Elemental composition and valence states were determined via X-ray photoelectron spectroscopy (XPS, ESCALAB 250Xi, Thermo Fisher, Waltham, MA, USA) under high vacuum conditions (>6 × 10^{-9} mbar). UV-Vis absorption spectra were recorded on a UV-Vis-NIR spectrophotometer (CARY500UV-VIS-NI, Varian, Palo Alto, CA, USA) to assess the optical absorption properties of the samples. Photoluminescence (PL) spectra were measured using a spectrometer (FLS100, Edinburgh, Livingston, UK) with an excitation wavelength of 310 nm to evaluate the separation efficiency of photogenerated carriers. Free radicals generated during the reaction were detected via electron param-

agnetic resonance (EPR) spectroscopy (EPR200 Plus, CIQTEK, Hefei, China) at X-band frequency (microwave frequency: 9.5 GHz; microwave power: 1 mW).

3.6. Electrochemical Measurements

Electrochemical properties were measured using a CHI 750E electrochemical workstation (Shanghai Chenhua Instrument Co., Ltd., Shanghai, China) in a standard three-electrode configuration. The working electrode was prepared by dropping a homogeneous suspension—containing 4 mg of catalyst, 30 μL of Nafion, 50 μL of isopropanol, and 200 μL of deionized water—onto fluorine-doped SnO_2 (FTO) glass (Yingkou OPV Tech New Energy Co., Ltd., Yingkou, China) with an active area of 1 cm^2. An Ag/AgCl electrode and a carbon electrode were used as the reference and counter electrodes, respectively, with 1 M $NaSO_4$ solution serving as the electrolyte. The semiconductor energy band structure was determined using Mott–Schottky plots, photogenerated carrier generation was evaluated using photocurrent response curves, and electron transfer resistance was analyzed via electrochemical impedance spectroscopy (EIS).

3.7. Photocatalytic Reduction of CO_2

The catalyst was coated onto a circular glass sheet (China Luoyang Float Glass Group Co., Ltd., Luoyang, China, diameter: 5 cm, thickness: 4.5 mm) for photocatalytic experiments. A specific amount of g-C_3N_4, $ZnIn_2S_4$, or $ZnIn_2S_4$/g-C_3N_4 was mixed with 2 mL of C_2H_5OH and ultrasonicated for 5 min. The suspension was then evenly spread on quartz glass and dried at 60 °C until all C_2H_5OH evaporated.

For a typical photocatalytic reaction, 20 mL of deionized water was added to an 80 mL gas cylinder, which was connected to a sealed 250 mL glass reactor covered with quartz glass. The circular glass sheet with the catalyst was placed flat in the reactor, ensuring the catalyst side faced upward. Prior to illumination, high-purity CO_2 was bubbled into the reactor for 30 min to expel air and create a CO_2 atmosphere. A 300 W xenon lamp (CEL-HXF300, Beijing China Education Au-light Co., Ltd., Beijing, China) served as the light source. The gas products (CO and H_2) were analyzed and quantified every 30 min using a gas chromatograph (GC, PANNA A60 with a thermal conductivity detector and a flame ionization detector, a 5A packed column, a box temperature of 50 °C, an inlet temperature of 380 °C, and N_2 as the carrier gas, Panna Instruments Co., Ltd., Changzhou, China). The total product yield was calculated by summing the detected values over an 8h reaction period [43,44]. The flow chart for photocatalytic CO_2 reduction is presented in Scheme 2.

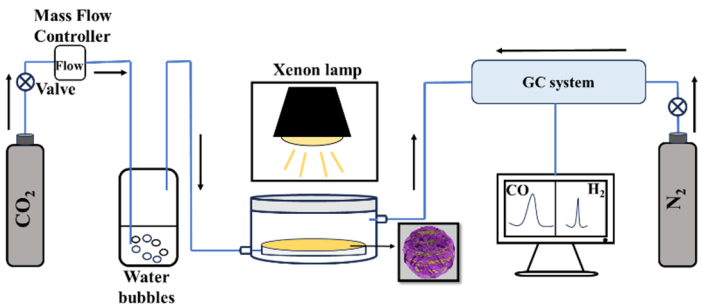

Scheme 2. Detailed flow chart of the photocatalytic CO_2 reduction process.

4. Conclusions

In this study, a novel $ZnIn_2S_4$/g-C_3N_4 heterojunction photocatalyst was successfully synthesized and demonstrated excellent performance for the photocatalytic reduction of CO_2. Compared to pristine g-C_3N_4 and $ZnIn_2S_4$, the composite exhibited significantly

enhanced separation and transfer efficiency in photogenerated charge carriers, leading to a substantial improvement in photocatalytic CO_2 reduction efficiency. Under 8 h of irradiation, the composite achieved a maximum total yield of CO at 3743.14 μmol·g^{-1}, 1.92 and 5.83 times higher than that of pristine g-C_3N_4 (1941.49 μmol·g^{-1}) and $ZnIn_2S_4$ (641.68 μmol·g^{-1}), along with a remarkable CO selectivity of 91.3%. Furthermore, this study confirmed a Z-scheme charge transfer pathway in the $ZnIn_2S_4$/g-C_3N_4 heterojunction, which preserved the strong redox capabilities of the charge carriers, resulting in superior photocatalytic performance. These findings highlight the potential of $ZnIn_2S_4$/g-C_3N_4 as a highly active, stable, and durable Z-scheme heterojunction photocatalyst for solar-driven chemical energy conversion. This work provides valuable insights into the design of advanced photocatalysts for sustainable energy applications.

Author Contributions: J.F.: Data Management; Methodology; Survey; Writing—original drafts; M.W.: Methodology; Visualization; X.Y.: Visualization; Q.S.: Resources; Writing—review and editing; and L.Y.: Resources; Supervision. All authors have read and agreed to the published version of the manuscript.

Funding: This work was partially supported by the National Natural Science Foundation of China (51402161 and 21776147) and the Natural Science Foundation of Qingdao (24-4-4-zrjj-178-jch).

Data Availability Statement: The data will be made available on request.

Conflicts of Interest: The authors declare no conflicts of interest.

References

1. Li, D.; Kassymova, M.; Cai, X.; Zang, S.; Jiang, H. Photocatalytic CO_2 reduction over metal-organic framework-based Materials. *Coord. Chem. Rev.* **2020**, *412*, 213262. [CrossRef]
2. Chu, S.; Cui, Y.; Liu, N. The path towards sustainable energy. *Nat. Mater.* **2017**, *16*, 16. [CrossRef] [PubMed]
3. Fu, J.; Jiang, K.; Qiu, X.; Yu, J.; Liu, M. Product selectivity of photocatalytic CO_2 reduction reactions. *Mater. Today.* **2020**, *32*, 222. [CrossRef]
4. Zhao, G.; Hu, J.; Long, X.; Zou, J.; Yu, J.; Jiao, F. A Critical Review on Black Phosphorus-Based Photocatalytic CO_2 Reduction Application. *Small* **2021**, *17*, 2102155. [CrossRef]
5. Wang, L.; Yu, J. CO_2 capture and in situ photocatalytic reduction. *Chem Catalysis* **2022**, *2*, 428. [CrossRef]
6. Zhang, J.; Jiang, J.; Lei, Y.; Liu, H.; Tang, X.; Yi, H.; Huang, X.; Zhao, S.; Zhou, Y.; Gao, F. Photocatalytic CO_2 reduction reaction: Influencing factors, reaction pathways and dominant catalysts. *Sep. Purif. Technol.* **2024**, *328*, 125056. [CrossRef]
7. Fang, J.; Zhu, C.; Hu, H.; Li, J.; Li, L.; Zhu, H.; Mao, J. Progress of photocatalytic CO_2 reduction toward multi-carbon Products. *Sci. China-Chem.* **2024**, *67*, 1. [CrossRef]
8. Wang, W.; Wang, L.; Su, W.; Xing, Y. Photocatalytic CO_2 reduction over copper-based materials: A review. *J CO2 Util.* **2022**, *61*, 102056. [CrossRef]
9. He, Y.; Yin, L.; Yuan, N.; Zhang, G. Adsorption and activation, active site and reaction pathway of photocatalytic CO_2 reduction: A review. *Chem. Eng. J.* **2024**, *481*, 148754. [CrossRef]
10. Qu, T.; Wei, S.; Xiong, Z.; Zhang, J.; Zhao, Y. Progress and prospect of CO_2 photocatalytic reduction to methanol. *Fuel Process. Technol.* **2023**, *251*, 107933. [CrossRef]
11. Idrees, F.; Butt, F.K.; Hammouda, S.B. Progression in Photocatalytic Materials for Efficient Performance. *Catalysts* **2021**, *11*, 472. [CrossRef]
12. Li, F.; Xiao, X.; Zhao, C.; Liu, J.; Li, Q.; Guo, C.; Tian, C.; Zhang, L.; Hu, J.; Jiang, B. TiO_2-on-C_3N_4 double-shell microtubes: In-situ fabricated heterostructures toward enhanced photocatalytic hydrogen evolution. *J. Colloid Interface Sci.* **2020**, *572*, 22. [CrossRef] [PubMed]
13. Zhao, P.; Jin, B.; Zhang, Q.; Peng, R. Graphitic-C_3N_4 quantum dots modified FeOOH for photo-Fenton degradation of organic pollutants. *Appl. Surf. Sci.* **2022**, *586*, 152792. [CrossRef]
14. Tao, W.; Tang, Q.; Hu, J.; Wang, Z.; Jiang, B.; Xiao, Y.; Song, R.; Guo, S. Construction of a hierarchical BiOBr/C_3N_4 S-scheme heterojunction for selective photocatalytic CO_2 reduction towards CO. *J. Mater. Chem. A* **2023**, *11*, 24999. [CrossRef]
15. Long, Z.; Yang, X.; Huo, X.; Li, X.; Qi, Q.; Bian, X.; Wang, Q.; Yang, F.; Yu, W.; Jiang, L. Bioinspired Z-scheme In_2O_3/C_3N_4 heterojunctions with tunable nanorod lengths for enhanced photocatalytic hydrogen evolution. *Chem. Eng. J.* **2023**, *461*, 141893. [CrossRef]

16. Song, Z.; Chen, Q.; Sun, Z.; Chang, K.; Xie, Z.; Kuang, Q. Constructing Z-scheme WO_3/C_3N_4 heterojunctions with an enlarged internal electric field and accelerated water oxidation kinetics for robust CO_2 photoreduction. *J. Mater. Chem. A* **2024**, *12*, 14426. [CrossRef]
17. Luo, F.; Liu, M.; Zheng, M.; Li, Q.; Wang, H.; Zhou, J.; Jiang, Y.; Yu, Y.; Jiang, B. Boosted charge separation in direct Z-scheme heterojunctions of $CsPbBr_3$/Ultrathin carbon nitride for improved photocatalytic CO_2 reduction. *J. Mater. Chem. A* **2023**, *11*, 241. [CrossRef]
18. Zheng, X.; Song, Y.; Liu, Y.; Yang, Y.; Wu, D.; Yang, Y.; Feng, S.; Li, J.; Liu, W.; Shen, Y.; et al. $ZnIn_2S_4$-based photocatalysts for photocatalytic hydrogen evolution via water splitting. *Coord. Chem. Rev.* **2023**, *475*, 214898. [CrossRef]
19. Li, Y.; Li, Z.; Liu, E. Preparation of $NiMoO_4/ZnIn_2S_4$ S-scheme Heteroiunctions and Enhancement Mechanism of Photocatalytic Hydrogen Production. *J. Liaocheng Univ. Nat. Sci. Ed.* **2023**, *36*, 1. [CrossRef]
20. Lu, Y.; Zou, X.; Wang, L.; Geng, Y. Preparation and Hydrogen Evolution Properties of $ZnIn_2S_4$/g-C_3N_4/MoS_2 Ternary Heterojunctions. *J. Liaocheng Univ. Nat. Sci. Ed.* **2023**, *36*, 57. [CrossRef]
21. Bi, Z.; Guo, R.; Hu, X.; Wang, J.; Chen, X.; Pan, W. Fabrication of a Concave Cubic Z-Scheme $ZnIn_2S_4/Cu_2O$ Heterojunction with Superior Light-Driven CO_2 Reduction Performance. *Energy Fuels* **2023**, *37*, 6036. [CrossRef]
22. Chen, C.; Du, S.; Wang, Y.; Han, Z.; Zhang, S.; Ma, W.; Zhang, Z.; Xu, H.; Fang, P. N-doped carbon-coated $CoSe_2/ZnIn_2S_4$ Z-scheme heterojunction for enhanced visible-light photocatalytic performances. *Int. J. Hydrogen Energy* **2024**, *90*, 1140. [CrossRef]
23. Shao, B.; Wang, J.; Zhang, Y.; Tan, X.; Zhou, W.; Chen, Y.; Xie, T.; Yu, T. Construction of a 3D/2D g-$C_3N_4/ZnIn_2S_4$ hollow spherical heterostructure for efficient CO_2 photoreduction under visible light. *Catal. Sci. Technol.* **2021**, *11*, 1282. [CrossRef]
24. Chen, K.; Wang, X.; Li, Q.; Feng, Y.; Chen, F.; Yu, Y. Spatial distribution of $ZnIn_2S_4$ nanosheets on g-C_3N_4 microtubes promotes photocatalytic CO_2 reduction. *Chem. Eng. J.* **2021**, *418*, 129476. [CrossRef]
25. Tan, M.; Ma, Y.; Yu, C.; Luan, Q.; Li, J.; Liu, C.; Dong, W.; Su, Y.; Qiao, L.; Gao, L.; et al. Boosting Photocatalytic Hydrogen Production via Interfacial Engineering on 2D Ultrathin Z-Scheme $ZnIn_2S_4$/g-C_3N_4 Heterojunction. *Adv. Funct. Mater.* **2022**, *32*, 2111740. [CrossRef]
26. Pan, X.; Shang, C.; Chen, Z.; Jin, M.; Zhang, Y.; Zhang, Z.; Wang, X.; Zhou, G. Enhanced Photocatalytic H_2 Evolution over $ZnIn_2S_4$ Flower-Like Microspheres Doped with Black Phosphorus Quantum Dots. *Nanomaterials* **2019**, *9*, 1266. [CrossRef]
27. Hezam, A.; Peppel, T.; Strunk, J. Pathways towards a systematic development of Z-scheme photocatalysts for CO_2 reduction. *Curr. Opin. Green Sust.* **2023**, *41*, 100789. [CrossRef]
28. Zhang, L.; Zhang, J.; Yu, H.; Yu, J. Emerging S-scheme photocatalyst. *Adv. Mater.* **2022**, *34*, 2107668. [CrossRef]
29. Liu, X.; Kang, S.; Yang, G.; Wang, Z.; Gao, G.; Dou, M.; Yang, H.; Li, R.; Li, D.; Dou, J. Interface regulation of $ZnIn_2S_4$/g-C_3N_4 S-scheme heterojunction for revealing exciton transfer mechanism and enhancing photocatalytic performance. *Int. J. Hydrogen Energy* **2024**, *51*, 410. [CrossRef]
30. Tan, P.; Zhang, M.; Yang, L.; Ren, R.; Zhai, H.; Liu, H.; Chen, J.; Pan, J. Modulated band structure in 2D/2D $ZnIn_2S_4$/B-C_3N_4 S-scheme heterojunction for photocatalytic hydrogen evolution. *Diamond Relat. Mater.* **2023**, *140*, 110456. [CrossRef]
31. Zhang, G.; Zhu, X.; Chen, D.; Li, N.; Xu, Q.; Li, H.; He, J.; Xu, H.; Lu, J. Hierarchical Z-scheme g-C_3N_4/Au/$ZnIn_2S_4$ photocatalyst for highly enhanced visible-light photocatalytic nitric oxide removal and carbon dioxide conversion. *Environ. Sci-Nano* **2020**, *7*, 676. [CrossRef]
32. Truc, N.; Bach, L.; Hanh, N.; Pham, T.; Le Chi, N.; Tran, D.; Nguyen, M. The superior photocatalytic activity of Nb doped TiO_2/g-C_3N_4 direct Z-scheme system for efficient conversion of CO_2 into valuable fuels. *J. Colloid Interface Sci.* **2019**, *540*, 1. [CrossRef] [PubMed]
33. Truc, N.; Hanh, N.; Nguyen, M.; Le Chi, N.; Van Noi, N.; Tran, D.; Ha, M.; Pham, T. Novel direct Z-scheme $Cu_2V_2O_7$/g-C_3N_4 for visible light photocatalytic conversion of CO_2 into valuable fuels. *Appl. Surf. Sci.* **2018**, *457*, 968. [CrossRef]
34. Guo, S.; Yang, P.; Zhao, Y.; Yu, X.; Wu, Y.; Zhang, H.; Yu, B.; Han, B.; George, M.; Liu, Z. Direct Z-Scheme Heterojunction of SnS_2/Sulfur-Bridged Covalent Triazine Frameworks for Visible-Light-Driven CO_2 Photoreduction. *ChemSusChem* **2020**, *13*, 6278. [CrossRef]
35. He, W.; Jia, H.; Wamer, W.; Zheng, Z.; Li, P.; Callahan, J.; Yin, J. Predicting and identifying reactive oxygen species and electrons for photocatalytic metal sulfide micro-nano structures. *J. Catal.* **2014**, *320*, 97. [CrossRef]
36. Zheng, Z.; Du, T.; Chen, P.; Yue, Q.; Wang, H.; Zhou, L.; Wang, Y. 2D/1D nested hollow porous $ZnIn_2S_4$/g-C_3N_4 heterojunction based on morphology modulation for photocatalytic CO_2 reduction. *J. Environ. Chem. Eng.* **2024**, *12*, 112971. [CrossRef]
37. Qiu, X.; Li, J.; Zhao, Y.; Lin, S.; Sun, Z.; Fang, Y.; Guo, L. The formation of Z-scheme AgI/BiOBr heterojunction and its excellent photocatalytic performance. *J. Alloys Compd.* **2023**, *967*, 171739. [CrossRef]
38. Ge, W.; Song, J.; Deng, S.; Liu, K.; Yang, P. Construction of Z-scheme $CoFe_2O_4$@$ZnIn_2S_4$ p-n heterojunction for enhanced photocatalytic hydrogen production. *Sep. Purif. Technol.* **2024**, *328*, 125059. [CrossRef]
39. Wang, G.; Tang, W.; Xu, C.; He, J.; Zeng, Q.; Xie, W.; Gao, P.; Chang, J. Two-dimensional CdO/PtSSe heterojunctions used for Z-scheme photocatalytic water-splitting. *Appl. Surf. Sci.* **2022**, *599*, 153960. [CrossRef]

40. Wang, K.; Huang, Z.; Wang, J. Synthesis of hierarchical tandem double Z-scheme heterojunctions for robust photocatalytic H_2 generation. *Chem. Eng. J.* **2022**, *430*, 132727. [CrossRef]
41. Wu, X.; Cheng, J.; Li, X.; Li, Y.; Lv, K. Enhanced Visible Photocatalytic Oxidation of NO by Repeated Calcination of g-C_3N_4. *Appl. Surf. Sci.* **2019**, *465*, 1037. [CrossRef]
42. Ma, G.; Shang, C.; Jin, M.; Shui, L.; Meng, Q.; Zhang, Y.; Zhang, Z.; Liao, H.; Li, M.; Chen, Z.; et al. Amorphous Ti(IV)-modified Flower-like $ZnIn_2S_4$ Microspheres with Enhanced Hydrogen Evolution Photocatalytic Activity and Simultaneous Wastewater Purification. *J. Mater. Chem. C* **2020**, *8*, 2693. [CrossRef]
43. Han, Q.; Li, L.; Gao, W.; Shen, Y.; Wang, L.; Zhang, Y.; Wang, X.; Shen, Q.; Xiong, Y.; Zhou, Y.; et al. Elegant Construction of $ZnIn_2S_4/BiVO_4$ Hierarchical Heterostructures as Direct Z-Scheme Photocatalysts for Efficient CO_2 Photoreduction. *ACS Appl. Mater. Interfaces* **2021**, *13*, 15092. [CrossRef] [PubMed]
44. Yang, S.; Sa, R.; Zhong, H.; Lv, H.; Yuan, D.; Wang, R. Microenvironments Enabled by Covalent Organic Framework Linkages for Modulating Active Metal Species in Photocatalytic CO_2 Reduction. *Adv. Funct. Mater.* **2022**, *32*, 2110694. [CrossRef]